

Optics Letters

Integrated broadband Ce:YIG/Si Mach–Zehnder optical isolators with over 100 nm tuning range

DUANNI HUANG,^{1,*†} PAOLO PINTUS,^{1,†} YUYA SHOJI,² PAUL MORTON,³ TETSUYA MIZUMOTO,²
AND JOHN E. BOWERS¹

¹Department of Electrical and Computer Engineering, University of California, Santa Barbara, California 93106, USA

²Department of Electrical and Electronic Engineering/FIRST, Tokyo Institute of Technology, Tokyo, Japan

³Morton Photonics, 3301 Velvet Valley Dr., West Friendship, Maryland 21794, USA

*Corresponding author: duanni@umail.ucsb.edu

Received 14 August 2017; revised 29 October 2017; accepted 2 November 2017; posted 3 November 2017 (Doc. ID 304738);
published 22 November 2017

We demonstrate integrated optical isolators with broadband behavior for the standard silicon-on-insulator platform. We achieve over 20 dB of optical isolation across 18 nm of optical bandwidth. The isolator is completely electrically controlled and does not require a permanent magnet. Furthermore, we demonstrate the ability to tune the central operating wavelength of the isolator across 100 nm, which covers the entire S + C telecom bands. These devices show promise for integration in optical systems in which broadband isolation is needed such as wavelength multiplexed systems or optical sensors. © 2017 Optical Society of America

OCIS codes: (230.3240) Isolators; (230.3810) Magneto-optic systems; (130.3120) Integrated optics devices.

<https://doi.org/10.1364/OL.42.004901>

Nonreciprocal optical devices [1] such as isolators and circulators are widely used in fiber optic communication systems, optical sensors, radio frequency photonics systems, and interconnects. The rapid growth of silicon photonics and growing complexity of photonic integrated circuits (PICs) need integrated isolators to ensure stable, high-performance laser operation. While considerable research effort has been performed to use dynamic modulation [2–4] or optical nonlinearities [5–7], the best results to date in terms of isolation ratio and optical bandwidth (BW) have used the magneto-optic effect to break reciprocity [8,9]. In particular, cerium substituted yttrium iron garnet (Ce:YIG) has been used due to its high Faraday rotation ($\theta_f = -4500$ deg/cm) at 1550 nm [10]. Deposition of Ce:YIG directly onto silicon is a promising approach, but is challenging due to the large thermal and lattice mismatch with silicon [11–14]. Alternatively, wafer bonding circumvents these issues and ensures optimal material quality, since the Ce:YIG is grown on a lattice-matched substituted gadolinium gallium garnet (SGGG) substrate [15–20]. While wafer-bonded approaches generally operate for the transverse magnetic (TM) polarization of light, they can be integrated with a polarization

rotator to be compatible with typical semiconductor lasers, which emit in the transverse electric polarization [17].

Previously, we have demonstrated microring-based optical isolators and circulators for silicon photonics with the wafer bonding approach [18]. Due to the small footprint of the devices, we used an integrated electromagnet deposited on the device to provide the necessary magnetic fields in highly localized areas on a chip instead of packaging a bulky permanent magnet. Additionally, the electromagnet can be used to tune the operating wavelength of the device and reconfigure the order of circulation of light through the circulator device [19]. While we achieved up to 32 dB of optical isolation, the device is intrinsically narrowband due to the ring architecture [20].

In this Letter, we extend our approach to Mach–Zehnder interferometer (MZI)-based isolators and demonstrate over 20 dB of optical isolation across 18 nm of BW. MZI devices have broadband performance when properly designed with a large free spectral range (FSR) [21]. By incorporating an integrated electromagnet instead of a permanent magnet, we also unlock the ability to tune the center wavelength of the isolator over 100 nm, a range that is only limited by the tuning range of our laser. Tunability is important, as the operating wavelength of a PIC should not be determined by the isolator. This tunability can also be used to adjust for temperature variation in the operation of the PIC and maintain the central isolation wavelength.

The design of our isolator begins with optimization of the cross section of a magneto-optic waveguide using a finite element mode solver to provide a nonreciprocal phase shift (NRPS) effect between forward and backward propagating light [22,23]. Depicted in Fig. 1, the cross section consists of Ce:YIG bonded on a patterned silicon-on-insulator wafer. The silicon waveguide is 220 nm tall by 600 nm wide and supports a single mode for the TM polarization. We directly bond the Ce:YIG onto the waveguide and proceed to thin down the SGGG substrate to 10 μm using mechanical polishing techniques. Finally, Ti/Au microstrips are deposited on the backside of the SGGG substrate to form the electromagnet. Further details concerning the fabrication flow can be found in Ref. [20].

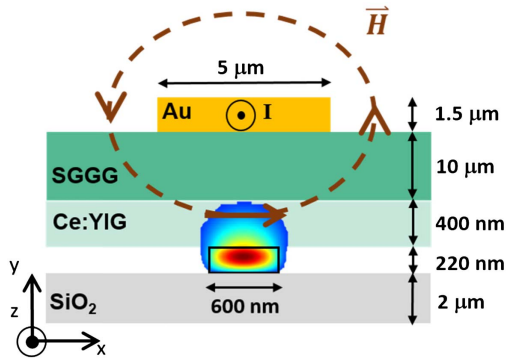


Fig. 1. Cross section of the fabricated waveguide with the fundamental TM mode overlaid.

To achieve optical isolation using NRPS, we form an unbalanced MZI, as shown in Fig. 2. Two electromagnets of equal length L are deposited on the arms and driven independently with opposite current polarity in a push-pull configuration. In this letter, we use directional couplers to split the light and analyze transmission in the cross state (Port 1 \rightarrow 4 and vice versa). 1×2 splitters and 3×2 couplers can be used instead. While the design in Fig. 2 can also be used as an optical circulator (Port 1 \rightarrow 4 \rightarrow 3 \rightarrow 2 \rightarrow 1), the wavelength dependence of the directional couplers prevents the device from being broadband. Adiabatic couplers are a possible option to ensure 50:50 splitting over a wide wavelength range [24]. In this Letter, we restrict the analysis of our device to an isolator, as the cross port of an MZI shows high extinction, regardless of the splitting ratio of the couplers if they are identical.

The optical path imbalance $\Delta\delta$ between the two arms is

$$\Delta\delta = \beta \cdot \Delta L + \beta_2 L - \beta_1 L, \quad (1)$$

where β is the phase constant of the waveguide when no magnetic field is present, β_1 and β_2 are the phase constants in the top and bottom arms, and ΔL is the geometrical path imbalance between the arms. When a current is injected through the electromagnet, the phase constant is changed by $\pm\delta\beta^{\text{MO}}$ due to

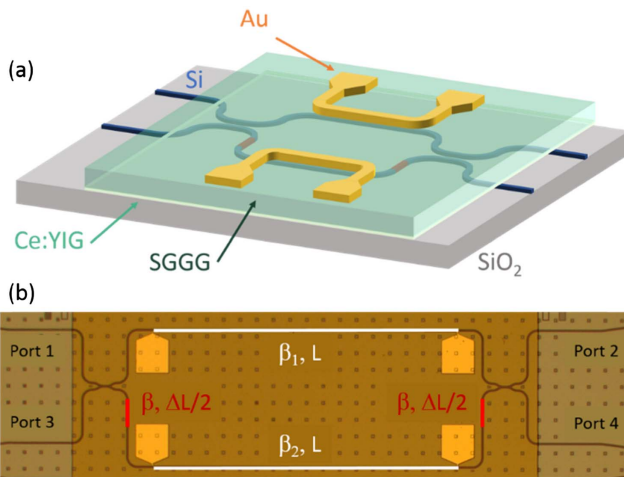


Fig. 2. (a) Schematic and (b) microscope image of the electromagnetically driven MZI isolator. The electromagnet and path imbalance are highlighted in white and red, respectively.

the magneto-optic NRPS, as well as $\delta\beta^{\text{TH}}$ due to Joule heating [18]. The sign of the magneto-optic effect is dependent on the direction of the magnetic field (and current), as well as the propagation direction of light. Assuming equal and opposite current I_1 and I_2 in the electromagnets, we obtain the following for β_1 and β_2 :

$$\beta_{1,\text{forward}} = \beta - \delta\beta^{\text{MO}} + \delta\beta^{\text{TH}}, \quad (2a)$$

$$\beta_{2,\text{forward}} = \beta + \delta\beta^{\text{MO}} + \delta\beta^{\text{TH}}, \quad (2b)$$

$$\beta_{1,\text{backward}} = \beta + \delta\beta^{\text{MO}} + \delta\beta^{\text{TH}}, \quad (2c)$$

$$\beta_{2,\text{backward}} = \beta - \delta\beta^{\text{MO}} + \delta\beta^{\text{TH}}. \quad (2d)$$

The thermal phase shift $\delta\beta^{\text{TH}}$ is the same for both arms if $\Delta L \ll L$, leaving only the magneto-optic effect to contribute to $\Delta\delta$. Finally, to achieve optical isolation, we need to satisfy the following equations:

$$\Delta\delta_{\text{forward}} = \beta \cdot \Delta L + 2\delta\beta^{\text{MO}} L = 2\pi m, \quad (3a)$$

$$\Delta\delta_{\text{backward}} = \beta \cdot \Delta L - 2\delta\beta^{\text{MO}} L = 2\pi n + \pi. \quad (3b)$$

This ensures that forward propagating light will interfere constructively at the coupler, while backward propagating light will interfere destructively. To minimize the size and, therefore, insertion loss of the device, we only consider $m = n + 1$. This selection results in $\delta\beta^{\text{MO}} L = \pi/4$, which determines the minimal length of the magneto-optic section, which has higher loss than standard silicon waveguides. From our simulations on this structure using a finite element-based mode solver [23], we obtain a conservative value $\delta\beta^{\text{MO}} = 0.834 \text{ mm}^{-1}$ and $\beta = 8.826 \mu\text{m}^{-1}$ for the fundamental TM mode at 1550 nm. This sets our electromagnet length at $L = 941 \mu\text{m}$. The reason for a conservative estimate is due to Joule heating, which decreases the magneto-optic effect [25]. In the absence of heating, $\delta\beta^{\text{MO}}$ can be as large as 2.294 mm^{-1} , meaning L can be as small as $342 \mu\text{m}$, which could further reduce the loss of this device.

Although broadband operation requires small values for m and n to make the FSR as large as possible, the spectral characteristics of the device are better analyzed using a device with a larger ΔL , since multiple fringes can be measured. Figure 3 depicts the spectrum from a narrowband device with $m = 200$ and $n = 199$, corresponding to $\Delta L = 143 \mu\text{m}$ and an FSR of roughly 5 nm. The devices are characterized using a tunable laser (1460–1580 nm), the polarized light edge coupled into the TM mode of the device, and a power meter used to record the power. The excess loss of the device caused by the Ce:YIG is ~ 8 dB, as normalized to a reference silicon waveguide with the same length. The origin of this loss primarily comes from propagation loss through the Ce:YIG clad silicon waveguide (~ 5 dB), as well as the transition of the waveguide into the bonded area (~ 1 dB each). From comparison to a Ce:YIG clad waveguide without the MZI, we see that the directional couplers and extra path length in the bottom arm accounts for another ~ 1 dB of loss. Shrinking the length of the interferometer (L) could reduce the loss even further.

When no current is applied to either arm, the forward and backward spectra are aligned. As we increase the equal, but opposite, currents I_1 and I_2 in the electromagnets, we observe a wavelength split between the minima of the forward and backward spectra. When $|I_1| = |I_2| = 180 \text{ mA}$, the minima of the

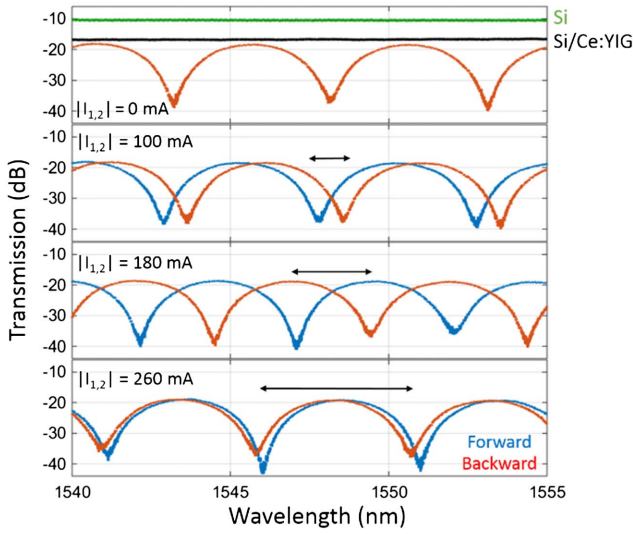


Fig. 3. Measured forward (blue) and backward (red) spectra for varying drive currents I_1 and I_2 that are equal, but opposite, in direction. The wavelength split (black arrow) grows with stronger current.

backward spectra align with the maxima of the forward spectra, which results in the maximum optical isolation. Given the 4 Ohm resistance of each microstrip, this corresponds to 130 mW of power dissipated due to the Joule heating per microstrip. Improvements on substrate removal to thin the SGGG even further will decrease the current required, since magnetic field strength is inversely proportional with substrate thickness. Decreasing the drive current will also help mitigate electromigration as a failure mechanism in the microstrip.

This is also depicted in Fig. 4, in which we plot the net phase difference in the interferometer between forward and backward propagation ($\Delta\delta_{\text{forward}} - \Delta\delta_{\text{backward}}$) for different driving currents. These values are extracted from analyzing the wavelength split versus the FSR of the MZI. As previously described in Eq. (3), we need a phase difference of π for optimal optical isolation, which is obtained near 180 mA. When the current is larger than 280 mA, we see a roll-off and saturation of the magneto-optic effect. This is because of a decrease in Faraday rotation due to Joule heating, as was also observed in our previous microring isolator devices [20].

To achieve broadband isolation, we reduce ΔL to 1.25 μm ($m = 2, n = 1$). Due to the large FSR, only a single fringe is

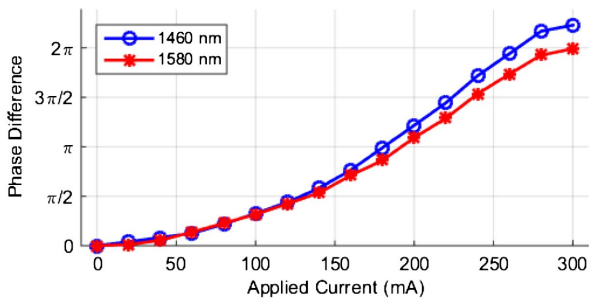


Fig. 4. Phase difference between forward and backward propagating light through the interferometer. The two curves track fringes of the MZI near 1460 and 1580 nm, respectively.

visible. Phase errors between the two arms blueshift the minimum of the spectra near 1450 nm instead of the designed 1550 nm, which is outside the range of our tunable laser. We can redshift the spectrum by slightly unbalancing the currents I_1 and I_2 , since the electromagnets can be controlled independently. However, doing so will also cause some thermal unbalance between the arms, and $\delta\beta^{\text{TH}}$ can no longer be ignored in Eq. (2). Experimentally, we see that the maxima of the forward spectra are not exactly aligned with the minima of the backward spectrum. Nevertheless, as long the unbalance is not too large, we can still observe significant optical isolation.

The best working conditions are shown in Fig. 5, where both the simulated and measured spectra are shown. We observe a maximum of 29 dB of isolation at 1523 nm, with an excess loss of ~ 9 dB, compared to our reference silicon waveguide. This is slightly higher than the narrowband device and may be a result of the imperfect phase conditions due to the unbalanced current. There are some ripples in the spectra, which are caused by reflections at the bonding interface. Care must be taken to provide a smooth transition into the Ce:YIG clad areas to avoid these spurious reflections. One option may be to use a silicon nitride cladding ($n = 2.0$) instead of silica cladding for waveguides outside the bonded region to better match the Ce:YIG ($n = 2.20$) and SGGG ($n = 1.97$). Alternatively, the waveguide can be widened at the interface to minimize the effective index mismatch.

When we sweep the current I_2 through the bottom, a longer arm from 200 to 240 mA, as shown in Fig. 6, the central wavelength for isolation continuously shifts to longer wavelengths. If we instead increase the current through the top shorter arm, the central wavelength will blueshift. In our device, the tuning mechanism is a combination of the thermal and magneto-optic effects since the effects are coupled. To further exploit this, we can introduce independent thermal heaters or use multiple coils for the electromagnet which will reduce the driving current required.

We calculate the isolation ratio (IR) for different isolation BW by using the following expression [18]:

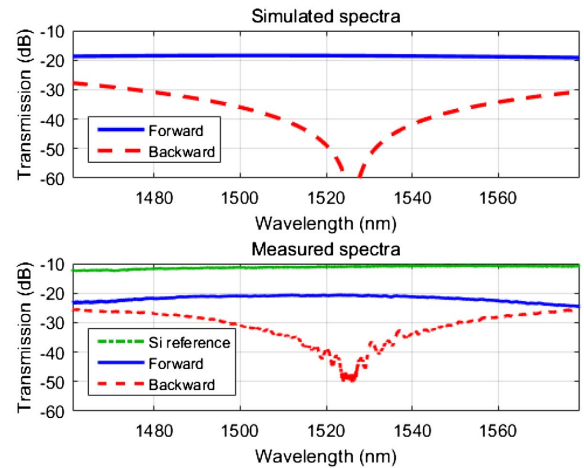


Fig. 5. Simulated and measured forward (continuous blue) and backward (dashed red) spectra for the broadband isolator when $|I_1| = 180$ mA and $|I_2| = 220$ mA.

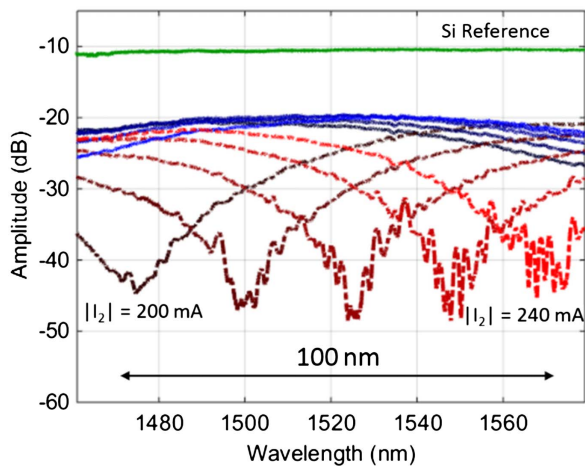


Fig. 6. Measured forward (blue) and backward (red) spectra for equally spaced driving current $|I_2|$ from 200 to 240 mA, while $|I_1|$ is kept at 180 mA. The minima of the backward spectra are shifted over 100 nm.

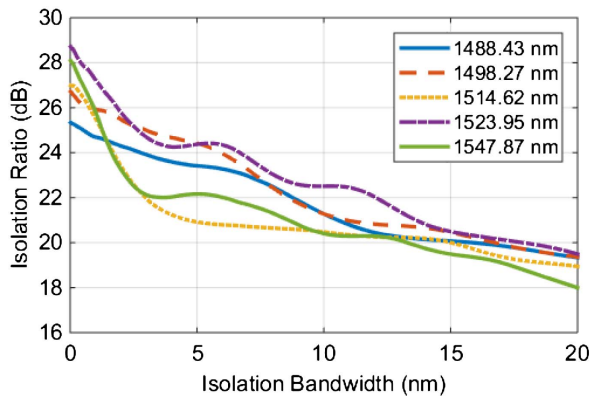


Fig. 7. Isolation ratio obtained versus isolation BW for different central isolation wavelengths.

$$IR(BW) = \frac{\int_{\lambda_0-BW/2}^{\lambda_0+BW/2} |S_{forw}(\lambda)| d\lambda}{\int_{\lambda_0-BW/2}^{\lambda_0+BW/2} |S_{back}(\lambda)| d\lambda} \quad (4)$$

In this equation, λ_0 is the central isolation wavelength, or the wavelength at which the minima of the backward spectra occur. Since the central wavelength is tuned as we adjust the current through the electromagnet, we repeat this calculation for different values of λ_0 . The results are shown in Fig. 7. We find that 20 dB of isolation ratio is guaranteed over 14 nm for the worst case ($\lambda_0 = 1547.87$ nm) and 18 nm for the best case ($\lambda_0 = 1523.95$ nm). While we were unable to measure isolation BW for spectra with minima near the limits of the tuning range of the laser, we expect similar performance across the whole 100 nm shown in Fig. 5. The excess loss ranges from 9 to 11 dB across the tuning range.

In conclusion, we demonstrate fully integrated optical isolators on silicon providing over 20 dB of isolation across 18 nm

of BW, with a maximum of 29 dB at 1523 nm. These isolators do not use a permanent magnet and can be electrically tuned over 100 nm without compromising device performance, covering the entire S and C bands in the telecom window. We believe that these devices present a promising approach to introduce broadband optical nonreciprocity to the silicon photonics platform.

Funding. Air Force (FA8650-16-C-1758).

Acknowledgment. The authors thank Jon Peters and M. J. Kennedy for fabrication assistance. They also thank Minh Tran, Chong Zhang, and Tin Komljenovic for helpful discussions.

[†]These authors contributed to this Letter equally.

REFERENCES

- D. Jalas, A. Petrov, M. Eich, W. Freude, S. Fan, Z. Yu, R. Baets, M. Popovic, A. Melloni, J. D. Joannopoulos, and M. Vanwolleghem, *Nat. Photonics* **7**, 579 (2013).
- H. Lira, Z. Yu, S. Fan, and M. Lipson, *Phys. Rev. Lett.* **109**, 033901 (2012).
- C. R. Doerr, L. Chen, and D. Vermeulen, *Opt. Express* **22**, 4493 (2014).
- M. J. Heck, S. Srinivasan, M. L. Davenport, and J. E. Bowers, *Photonics* **2**, 957 (2015).
- Y. Shi, Z. Yu, and S. Fan, *Nat. Photonics* **9**, 388 (2015).
- S. Hua, J. Wen, X. Jiang, Q. Hua, L. Jiang, and M. Xiao, *Nat. Commun.* **7**, 13657 (2016).
- C. H. Dong, Z. Shen, C. L. Zou, Y. L. Zhang, W. Fu, and G. C. Guo, *Nat. Commun.* **6**, 6193 (2015).
- B. J. Stadler and T. Mizumoto, *IEEE Photon. J.* **6**, 1 (2014).
- Y. Shoji, K. Miura, and T. Mizumoto, *J. Opt.* **18**, 013001 (2015).
- T. Shintaku and T. Uno, *J. Appl. Phys.* **76**, 8155 (1994).
- L. Bi, J. Hu, P. Jiang, D. H. Kim, G. F. Dionne, L. C. Kimerling, and C. A. Ross, *Nat. Photonics* **5**, 758 (2011).
- X. Y. Sun, Q. Du, T. Goto, M. C. Onbasli, D. H. Kim, N. M. Aimon, J. Hu, and C. A. Ross, *ACS Photon.* **2**, 856 (2015).
- A. D. Block, P. Dulal, B. J. Stadler, and N. C. Seaton, *IEEE Photon. J.* **6**, 1 (2014).
- P. Dulal, A. D. Block, T. E. Gage, H. A. Haldren, S. Y. Sung, D. Hutchings, and B. J. Stadler, *ACS Photon.* **3**, 1818 (2016).
- M. C. Tien, T. Mizumoto, P. Pintus, H. Kroemer, and J. E. Bowers, *Opt. Express* **19**, 11740 (2011).
- Y. Shoji, M. Ito, Y. Shirato, and T. Mizumoto, *Opt. Express* **20**, 18440 (2012).
- S. Ghosh, S. Keyvaninia, Y. Shirato, T. Mizumoto, G. Roelkens, and R. Baets, *IEEE Photon. J.* **5**, 6601108 (2013).
- P. Pintus, D. Huang, C. Zhong, Y. Shoji, T. Mizumoto, and J. E. Bowers, *J. Lightwave Technol.* **35**, 1429 (2017).
- D. Huang, P. Pintus, C. Zhong, Y. Shoji, T. Mizumoto, and J. E. Bowers, *Optica* **25**, 30 (2017).
- D. Huang, P. Pintus, C. Zhong, Y. Shoji, T. Mizumoto, and J. E. Bowers, *IEEE J. Sel. Top. Quantum Electron.* **22**, 4403408 (2016).
- Y. Shoji, Y. Shirato, and T. Mizumoto, *J. Appl. Phys.* **53**, 022202 (2014).
- P. Pintus, M. C. Tien, and J. E. Bowers, *IEEE Photon. Technol. Lett.* **23**, 1670 (2011).
- P. Pintus, *Opt. Express* **22**, 15737 (2014).
- H. Yun, W. Shi, Y. Wang, L. Chrostowski, and N. A. Jaeger, *Proc. SPIE* **8915**, 89150 (2013).
- K. Furuya, T. Nemoto, K. Kato, Y. Shoji, and T. Mizumoto, *J. Lightwave Technol.* **34**, 1699 (2016).